AGU PUBLICATIONS

JGR

Journal of Geophysical Research: Oceans

RESEARCH ARTICLE

10.1002/2017JC013561

A Study of Baroclinic Instability Induced Convergence Near the Bottom Using Water Age Simulations

Wenxia Zhang[1,2] and **Robert D. Hetland**[2]

[1]State Key Laboratory of Estuarine and Coastal Research, East China Normal University, Shanghai, China, [2]Department of Oceanography, Texas A&M University, College Station, TX, USA

Key Points:
- Convergence in response to eddy transport causes upward extension of bottom material
- Intensity of bottom tracer flux is determined by horizontal slope burger number
- Spatial patchiness in bottom oxygen concentrations is caused by eddy activity

Correspondence to:
W Zhang,
wenxia.zhang@sklec.ecnu.edu.cn

Citation:
Zhang, W., & Hetland, R. D. (2018). A study of baroclinic instability induced convergence near the bottom using water age simulations. *Journal of Geophysical Research: Oceans*, *123*, 1962–1977. https://doi.org/10.1002/2017JC013561

Received 20 OCT 2017
Accepted 26 JAN 2018
Accepted article online 1 FEB 2018
Published online 12 MAR 2018

Abstract Baroclinic instability of lateral density gradients gives way to lateral buoyancy transport, which often results in convergence of buoyancy transport. Along a sloping bottom, the induced convergence can force upward extension of bottom water. Eddy transport induced convergence at the bottom and the consequent suspended layers of bottom properties are investigated using a three-dimensional idealized model. Motivated by the distinct characteristics of intrusions over the Texas-Louisiana shelf, a series of configurations are performed with the purpose of identifying parameter impacts on the intensity of eddy transport. This study uses the "horizontal slope Burger number" as the predominant parameter; the parameter is functioned with $S_H = SRi^{-1/2} = \delta/Ri$ to identify formation of baroclinic instability, where S is the slope Burger number, δ is the slope parameter, and Ri is the Richardson number, previously shown to be the parameter that predicts the intensity of baroclinic instability on the shelf. Intrusion spreads into the interior abutting a layer that is characterized by degraded vertical stratification; a thickening in the bottom boundary layer colocates with the intrusion, which usually thins at either edge of the intrusion because of a density barrier in association with concentrated isopycnals. The intensity of convergence degrades and bottom tracer fluxes reduce linearly with increased S_H on logarithmic scales, and the characteristics of bottom boundary layer behavior and the reversal in alongshore current tend to vanish.

1. Introduction

Baroclinic instabilities are a ubiquitous feature of oceanic flows and can occur at variable scales in the ocean. Very small scale instabilities, confined within the mixed layer with typical spacing of 0.1–10 km, are often described as "submesoscale" (e.g., Hetland, 2016; McWilliams et al., 2009). The Rossby number, $Ro = U(fL)^{-1}$, at small scale $Ro \sim 1$, where U is the magnitude of horizontal current velocity, f is the Coriolis parameter, and L is the magnitude of horizontal length scale. Instabilities on the order of the deformation radius are considered as the most favorable to growth (e.g., Cushman-Roisin & Beckers, 2011), such that $Ro^2Ri \sim 1$, where the Richardson number $Ri = N^2U_z^2 = N^2f^2M^{-4}$ through thermal wind balance, and M^2 and N^2 are the magnitudes of the lateral and vertical buoyancy gradients, respectively (Hetland, 2016).

Baroclinic eddies are important agents of lateral transports of tracers such as nutrients and plankton, buoyancy, and mass (e.g., Cushman-Roisin & Beckers, 2011; Mahadevan & Archer, 2000; Siegel et al., 1999) in frontal regions, and also have important implications on biogeochemistry (Mahadevan & Archer, 2000; Mahadevan et al., 2012; Siegel et al., 1999; Smith et al., 2015). Patches and filaments of tracers in the submesoscale range can be seen globally, which are closely linked to episodic eddy transports (Capet et al., 2008a, 2008b, 2008c). Due to the spatiotemporally irregular and heterogeneous nature of baroclinic eddies, the resulting environment for tracers is rather patchy from a horizontal perspective (Mahadevan, 2014, 2016; Mahadevan et al., 2012). For instance, plankton patchiness in submesoscale range often occurs (e.g., Mahadevan, 2016; Smith et al., 2015), which can subsequently modulate predator distribution and abundance.

Lateral buoyancy transport, induced by the development of baroclinic instability, often forces localized convergent flows. McWilliams et al. (2009) identified eddy induced oceanic surface convergent zones in the submesoscale range, and these convergent zones often carry surface materials down into the interior. Similarly, at the bottom, convergence can form in response to baroclinic eddy induced lateral buoyancy transport, accompanied by upward spread of bottom materials. For instance, bottom convergence in response

to baroclinic eddies can incorporate nutrient-replete water into the euphotic zone, which triggers new primary production patchiness and comes into balance with the sinking of organic matter into the aphotic zone assuming that the marine ecosystem is at steady state from an annual time scale perspective (e.g., Mahadevan & Archer, 2000; Siegel et al., 1999). To understand the characteristics of baroclinic eddies, the means by which nutrients at relatively deep water can be transported upward into the euphotic zone, is of central importance for exploring ecosystem balance and biodiversity.

Suspended layers of bottom material in the interior are detected in different regions (e.g., Houghton & Visbeck, 1998; Pickart, 2000; Zhang et al., 2015) and are suggested to be upward extensions of bottom material that predominantly driven by convergence associated with Ekman buoyancy transport. Baroclinic eddies also induce buoyancy transport, which can cause a similar phenomenon in this study. In some regions, vertical velocities in association with frontal eddies can be orders of magnitude larger than that in association with Ekman pumping (e.g., Mahadevan & Archer, 2000). Therefore, it is necessary also important to investigate the vertical fluxes that induced by baroclinic instabilities exclusively. To quantitatively evaluate baroclinic instability of the lateral density gradients in regard to vertical material flux, simulations that excite eddy transport can be performed.

In this study, a simple three-dimensional model based on Regional Ocean Modeling System (ROMS) is performed, with the aim of identifying the characteristics of convergent flow in response to eddy transport and quantifying the consequent bottom material fluxes. The model setup is similar to what Hetland (2016) described yet this paper focuses on investigating vertical material fluxes in response to baroclinic eddy transport. The density surfaces are initially sloped through thermal wind relation. With a surface-intensified alongshore flow associated with the lateral density gradients, the system is subjective to baroclinic instability. Hence the model starts with a thermal wind balance yet has no external forcing to sustain the balance. Baroclinic instability grows and extracts potential energy from the ambient and tend to mix the water column. In agreement with previous studies (e.g., Haine & Marshall, 1998), ateral buoyancy transport in response to baroclinic eddies is efficient, and isopycnal slope shows significant reduction during the evolution of submesoscale eddies.

Hetland (2016) investigated suppression of baroclinic instabilities by introducing a new nondimensional parameter, "horizontal slope Burger number (S_H)," with the purpose of explaining rarely observed instabilities in river plumes. Hetland (2016) stated that a threshold value of $S_H \gtrsim 0.2$ constrains the formation of baroclinic instability with a few exceptions associated with initial $Ri = 1$, the states of which also evolve and instability can form yet is quite weak. Motivated by Hetland (2016), "horizontal slope Burger number" is used as the dominant parameter that controls the suppression of instability in this study. We find behavioral differences in regard to bottom material intrusions driven by convergent flows and simultaneous bottom boundary layer dynamics associated with different horizontal slope Burger number, and bottom fluxes decrease with increased S_H linearly on logarithmic scales.

2. Methodology

2.1. Model Description

A simple three-dimensional model that is similar to what Hetland (2016) described is used in this study. The model (Figure 2) has 30 vertical layers, with a minimum water depth of 5 m (h_0) at the coast and lying above a sloping bottom at $H = h_0 + \beta y$ with 1% random noise to regulate the topography, allowing the development of perturbation. The bottom slope, $\beta = 0.001$, is constant everywhere in the model domain. The horizontal resolution is 1 km with a domain size of 130 km in the alongshore direction and 130 km in the cross-shore direction. The model is a reentrant domain with periodic alongshore boundaries, closed coastal and open offshore boundaries. The three-dimensional variables for the offshore open boundary condition use a simple no-gradient condition. Sea surface height and barotropic currents use a Chapman/Flather combination (Chapman, 1985; Flather, 1976).

The ocean has a constant, horizontally uniform initial vertical stratification that is controlled by temperature exclusively throughout the domain. Inshore of 50 km, the ocean has a constant initial horizontal stratification controlled by salinity exclusively. Horizontal and vertical stratification are conservative through a linear equation of state, such that the horizontal and vertical density gradient can be explicitly formed through the combination of horizontal (salinity) and vertical stratification (temperature). The alongshore

Table 1
List of Parameters for Model Simulations

Run no.	$M^2(s^{-2})$	$N^2(s^{-2})$	$f(s^{-1})$	Ri	S_H	T_d
1	1.00×10^{-6}	1.00×10^{-4}	1.00×10^{-4}	1.0	0.1	31
2	9.00×10^{-7}	1.80×10^{-4}	6.71×10^{-5}	1.0	0.2	31
3	8.00×10^{-7}	2.40×10^{-4}	5.16×10^{-5}	1.0	0.3	31
4	6.19×10^{-7}	3.09×10^{-4}	3.52×10^{-5}	1.0	0.5	54
5	5.00×10^{-7}	4.17×10^{-4}	2.45×10^{-5}	1.0	0.83	132
6	4.00×10^{-7}	4.00×10^{-4}	2.00×10^{-5}	1.0	1.00	201
7	3.50×10^{-7}	5.46×10^{-4}	1.50×10^{-5}	1.0	1.56	151
8	2.14×10^{-7}	4.60×10^{-4}	1.00×10^{-5}	1.0	2.14	151
9	1.00×10^{-7}	4.00×10^{-4}	5.00×10^{-6}	1.0	4.00	151
10	8.38×10^{-8}	6.45×10^{-4}	3.30×10^{-6}	1.0	7.70	151
11	1.00×10^{-6}	1.00×10^{-4}	1.42×10^{-4}	2.0	0.05	31
12	9.00×10^{-7}	1.80×10^{-4}	9.49×10^{-5}	2.0	0.1	31
13	8.03×10^{-7}	2.41×10^{-4}	7.32×10^{-5}	2.0	0.15	31
14	6.00×10^{-7}	3.00×10^{-4}	4.90×10^{-5}	2.0	0.25	60
15	4.99×10^{-7}	4.16×10^{-4}	3.46×10^{-5}	2.0	0.42	120
16	1.00×10^{-6}	1.00×10^{-4}	1.74×10^{-4}	3.0	0.03	31
17	9.10×10^{-7}	1.82×10^{-4}	1.17×10^{-4}	3.0	0.07	31
18	8.00×10^{-7}	2.41×10^{-4}	8.94×10^{-5}	3.0	0.1	31
19	6.00×10^{-7}	3.00×10^{-4}	6.01×10^{-5}	3.0	0.17	50
20	5.00×10^{-7}	4.17×10^{-4}	4.25×10^{-5}	3.0	0.28	103
21	1.01×10^{-6}	1.02×10^{-4}	2.24×10^{-4}	5.0	0.02	31
22	9.00×10^{-7}	1.80×10^{-4}	1.50×10^{-4}	5.0	0.04	31
23	8.00×10^{-7}	2.42×10^{-4}	1.15×10^{-4}	5.0	0.06	31
24	6.00×10^{-7}	3.01×10^{-4}	7.74×10^{-5}	5.0	0.1	51
25	5.00×10^{-7}	4.18×10^{-4}	5.47×10^{-5}	5.0	0.17	92

Note. All simulations are performed with bottom slope $\beta=0.001$. T_d is the dimensional time that each case performed.

surface-intensified geostrophic flow initially comes into balance with the sloped density surfaces through thermal wind relation, and the ocean has no external forcing with available potential energy the only forcing in the system. Twenty-five simulations, spanning a range of parameters typical for the Texas-Louisiana shelf, are listed in Table 1. Note that all the cases are performed long enough to pass the dimensional time corresponding to $t'=50$, where t' is a normalized time:

$$t'=t\omega^*_{l\max}S^{-1/2}, \tag{1}$$

where t is the dimensional time, and $\omega^*_{l\max}=\omega_{l\max}f\,Ri^{-1}$ is based on the nondimensional time scale of fastest instability growth. The reader is referred to Hetland (2016) for more equations and the reason for choosing $t'=50$. The initial conditions in association with $Ri=1.0$ and $S_H=0.2$ (run 2 in Table 1) are shown in Figure 2.

2.2. Water Age

Water age cannot be observed directly, and usually transient tracers are used in numerical models to infer water age, which generally suggests the elapsed time since the water was last in contact with the tracer source. While it is common to define the age of water as the last contact with the surface, here we will define age as last contact with the seafloor, as this is more relevant to the investigation of bottom hypoxia.

Water age is computed following Delhez et al. (1999), Deleersnijder et al. (2001), Delhez and Deleersnijder (2006), and Zhang et al. (2010). Assuming that the position vector of a water parcel in the domain is $\mathbf{x}=(x,y,z)$. The equation that governs the evolution of the age distribution function, $c(t,\mathbf{x},\tau)$, of a water parcel containing dissolved tracer located at $\mathbf{x}$ at time t is

$$\frac{\partial c}{\partial t}=p-d-\nabla\cdot(\mathbf{u}c-\mathbf{K}\cdot\nabla c)-\frac{\partial c}{\partial \tau}, \tag{2}$$

where τ is the age (i.e., the time since the tracer was released into the water from the bottom in this study); p and d are the production and destruction rates, respectively (i.e., the source and sink terms; in this study,

production effectively enters the system only at the bottom); **u** is the current velocity; and **K** is the eddy diffusivity tensor. The last term on the right-hand side is related to the ageing of the tracer, i.e., the age of every water parcel tends to increase by a certain amount of time as time progresses by the same amount of time (Delhez et al., 1999).

Assuming that the age is positive definite, the concentration of tracer in the fluid is

$$C(t,\mathbf{x})=\int_0^\infty c(t,\mathbf{x},\tau)d\tau. \tag{3}$$

Then integrate equation (2) over τ, taking into account equation (3) and the common-sense boundary conditions, $\lim_{x\to\infty} c(t,\mathbf{x},\tau)=0$, to get the equation of the time rate of change of the total concentration of the tracer:

$$\frac{\partial C}{\partial t}=P-D-\nabla\cdot(\mathbf{u}C-\mathbf{K}\cdot\nabla C), \tag{4}$$

with the source of tracer $P(t,\mathbf{x})=c(t,\mathbf{x},\tau=0)+\int_0^\infty p(t,\mathbf{x},\tau)d\tau$ and the sink $D(t,\mathbf{x})=\int_0^\infty d(t,\mathbf{x},\tau)d\tau$. Equation (4) is the conservation equation solved in numerical models.

The mean age $a(t,\mathbf{x})$ is given based on the definition of the age distribution function,

$$a(t,\mathbf{x})=\frac{1}{C(t,\mathbf{x})}\int_0^\infty \tau c(t,\mathbf{x},\tau)d\tau. \tag{5}$$

An age concentration tracer, $\alpha(t,\mathbf{x})$, is defined as

$$\alpha(t,\mathbf{x})=C(t,\mathbf{x})a(t,\mathbf{x}), \tag{6}$$

and we apply a reasonable assumption that the age distribution function verifies $\lim_{x\to 0}\tau c(t,\mathbf{x},\tau)=0=\lim_{x\to\infty}\tau c(t,\mathbf{x},\tau)$. Then, multiplying equation (2) by τ, integrating over τ, we obtain the age concentration equation:

$$\frac{\partial \alpha}{\partial t}=C+\pi-\delta-\nabla\cdot(\mathbf{u}\alpha-\mathbf{K}\cdot\nabla\alpha), \tag{7}$$

with $\pi(t,\mathbf{x})=\int_0^\infty \tau p(t,\mathbf{x},\tau)d\tau$ and $\delta(t,\mathbf{x})=\int_0^\infty \tau d(t,\mathbf{x},\tau)d\tau$. So the age concentration α satisfies an equation similar to that governing the evolution of the concentration of tracer. The "mean age" *a* will be the "water age" in this study.

In the model, "water age" is introduced by activating two passive tracers at the bottom grid cell to track the paths of water masses. The two passive tracers are activated in the model with zero initial concentration. The first is conservative and satisfies equation (4) with the tracer source at the bottom layer with unity tracer concentration (per m^3), whereas the second represents the water age concentration and satisfies equation (7). Water age concentration is zero at the bottom, and water age is computed with equation (6). Regions where the first tracer concentration is lower than 10^{-4} are assumed to be free of bottom water, and the age there is undefined.

2.3. Convergent Flow Near the Bottom and Consequent Vertical Fluxes

To find the convergent zones within the bottom boundary layer over the shelf, first, flow through density surfaces for the bottom cell of the model is calculated using simulated results. In the ocean, the density equation is

$$\frac{\partial \rho}{\partial t}+\vec{u}\cdot\vec{\nabla}\rho=\vec{\nabla}\cdot\vec{F}. \tag{8}$$

In equation (8), ρ is the density field, $\vec{u}$ is the simulated current velocity vector, and $\vec{F}$ is the diffusivity term. The total current velocity vector near the bottom, $\vec{u}$, can be divided into three parts, the velocity of the density surface itself $\vec{u}_I$, the flow through the density surface $\vec{u}_M$, and the flow along the density surface $\vec{u}_P$ (Figure 1). Since the dot product of $\vec{u}_P$ and density gradient, $\vec{\nabla}\rho$, is zero, $\vec{u}_P$ can be ignored in the equation. In other words, $\vec{u}_I+\vec{u}_M$ is the normal component (in the sense of density surface) of bottom current velocity, $\vec{u}_c$. So, equation (8) can be rewritten as

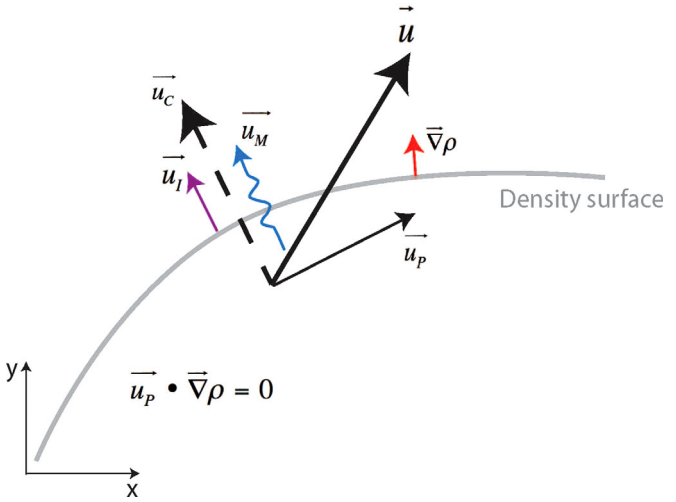

Figure 1. Sketch depicting flow near the bottom cell of the model. The gray line is a density surface, the thin black arrow represents current velocity along density surface, the dashed black arrow represents the cross-isopycnal component of water motion, the blue arrow represents flow through density surface and the purple arrow represents density surface motion near the bottom (equations (9) and (13)). The figure is adapted from Zhang et al. (2015).

$$\frac{\partial \rho}{\partial t} + (\vec{u}_I + \vec{u}_M) \cdot \vec{\nabla}\rho = \vec{\nabla} \cdot \vec{F}. \tag{9}$$

In equation (9), $\vec{u}_I$ is associated with inviscid motions and is reversible, which means the density surface itself can move on-shore and offshore as well as go back to its original location; $\vec{u}_M$ is associated with mixing and is irreversible. Such that, equation (9) can be divided into two components:

$$\frac{\partial \rho}{\partial t} + \vec{u}_I \cdot \vec{\nabla}\rho = 0, \tag{10}$$

and

$$\vec{u}_M \cdot \vec{\nabla}\rho = \vec{\nabla} \cdot \vec{F}. \tag{11}$$

Figure 1 shows the bottom layer in *x-y* plane; the gray line represents a density surface along the bottom. The isopycnal motions are estimated using equation (10) describing the motions of a density surface at the seafloor. Diffusion is ignored, because this equation follows the isopycnal surfaces instead of water parcels. The magnitude of isopycnal motion will be

$$u_I = \frac{\left|\frac{\partial \rho}{\partial t}\right|}{|\vec{\nabla}\rho|}. \tag{12}$$

The motion is perpendicular to the bottom density surface, and the direction of isopycnal motion depends on the sign of the $\frac{\partial \rho}{\partial t}$ term. Water motion near the bottom is calculated directly from the simulated current

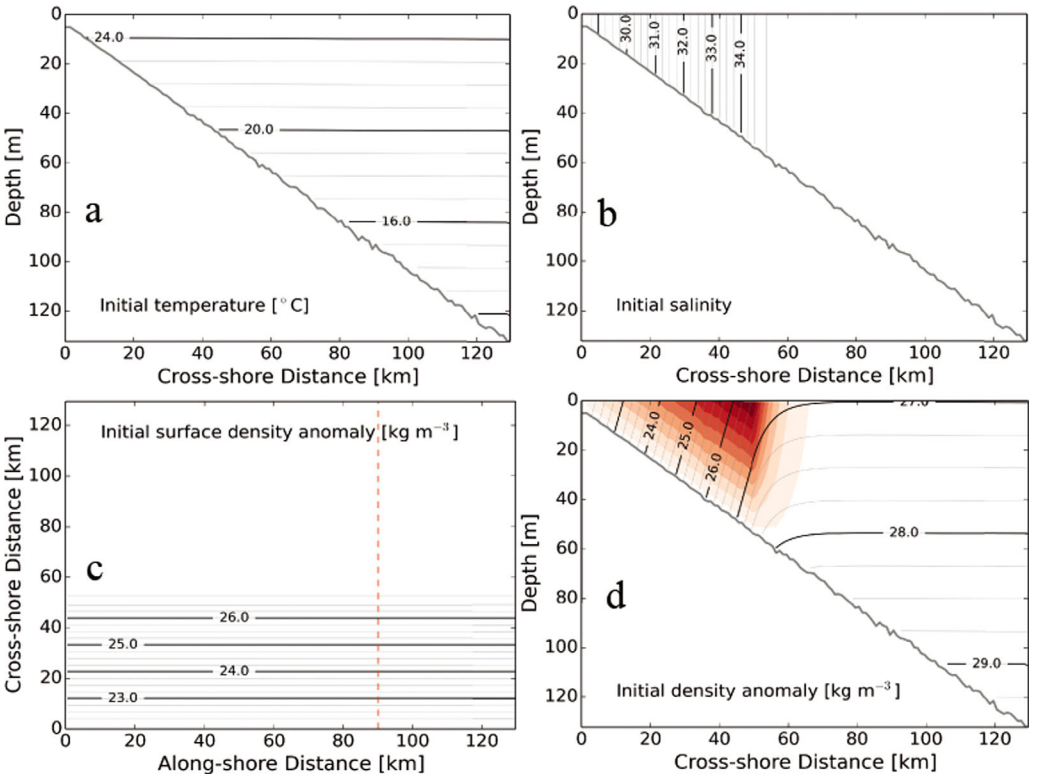

Figure 2. This figure shows the model domain, and initial structures of the cross-shelf temperature, salinity, isopycnal, and alongshore flow (red shading) in response to the sloped isopycnal via thermal wind relation for run 2 (see Table 1). The cross section is denoted by the red dashed line.

velocity in the bottom layer. Only the cross-isopycnal flow will advect or flow through the surface isopycnal, and the cross-isopycnal component of water motion is obtained using

$$\vec{u}_c = \frac{\vec{u} \cdot \vec{\nabla}\rho}{|\vec{\nabla}\rho|}. \tag{13}$$

In this equation, $\vec{u}_c$ represents the cross-isopycnal component of water motion, and $\frac{\vec{\nabla}\rho}{|\vec{\nabla}\rho|}$ is the unit vector perpendicular to the isopycnal surface. The flow through density surface is obtained by subtracting the isopycnal motion near the bottom from cross-isopycnal component of water motion:

$$\vec{u}_M = \frac{\vec{u} \cdot \vec{\nabla}\rho}{|\vec{\nabla}\rho|} - \vec{u}_l. \tag{14}$$

Instead of the strength of mixing, our interest in this study is the convergence of the flow, relative to the density surfaces, which will then be

$$\xi = \vec{\nabla} \cdot (\vec{u}_c - \vec{u}_l). \tag{15}$$

Following equation (15), the convergence near the bottom cell can be computed. Then cast convergence into a density coordinate. The density coordinate is a coordinate system that follows density coordinates and is less sensitive to the geographical location of the convergence. By identifying regions of persistently convergent flow in a particular range of isopycnals, regions where water is injected into the interior water column can be identified. This metric considers the water mass structure of the convergence as a whole, identifying the isopycnal where convergence occurs. The readers are referred to (Zhang et al., 2015) for detailed explanations.

The upward tracer flux through a reference plane A is expressed as

$$F = \int_A \mathbf{w}C \cdot d\mathbf{A}, \tag{16}$$

with positive values of the velocity that is normal to the reference plane (the sum of the normal components of velocities along y and z axis), $\mathbf{w}$, tracer concentration, C, and the corresponding area, $d\mathbf{A}$. The values of the velocity and tracer concentration vary with δh, the distance between the bottom and the reference plan A. Net tracer flux, net amount of substance that moves through the reference plane, is also quantified in the same way.

2.4. Parameter Description

Hetland (2016) found that the "horizontal slope Burger number" controls the suppression of instabilities in the idealized simulations presented, which defines the initial partitioning of kinetic to available potential energy:

$$S_H = \frac{M^2\beta}{f^2} = \frac{S}{Ri^{1/2}} = \frac{\delta}{Ri} = \frac{\text{Initial Mean Kinetic Energy}}{\text{Initial Available Potential Energy}}, \tag{17}$$

where $S = Nf^{-1}\beta$ is the slope Burger number that used to examine the influence of stratification on a sloping shelf (Brink & Lentz, 2010a), and $\delta = N^2M^{-2}\beta$ is the slope parameter. These two parameters together with Ri are related through the relation $\delta = Ri^{1/2}S$. In this study, S_H is adjusted over a series of numerical simulations to create a variable amount of eddy activity in order to investigate the role of these eddies on biological tracers.

3. Results

3.1. Isopycnal Motion

Figure 2 shows the initial state of run 2; baroclinic instabilities evolve over time and Figure 3 shows a variety of evolution stages for bottom, surface, and transects of density distributions. The motion of isopycnal is associated with the slumping of the initially sloped density surfaces. Baroclinic eddies evolve spatiotemporally and transects of density distributions illustrate that isopycnal 27 kg/m^3 shifts seaward from 58 to 71 km at the surface and shoreward from 45 to 35 km at the bottom in 16 days. The shifting of isopycnal

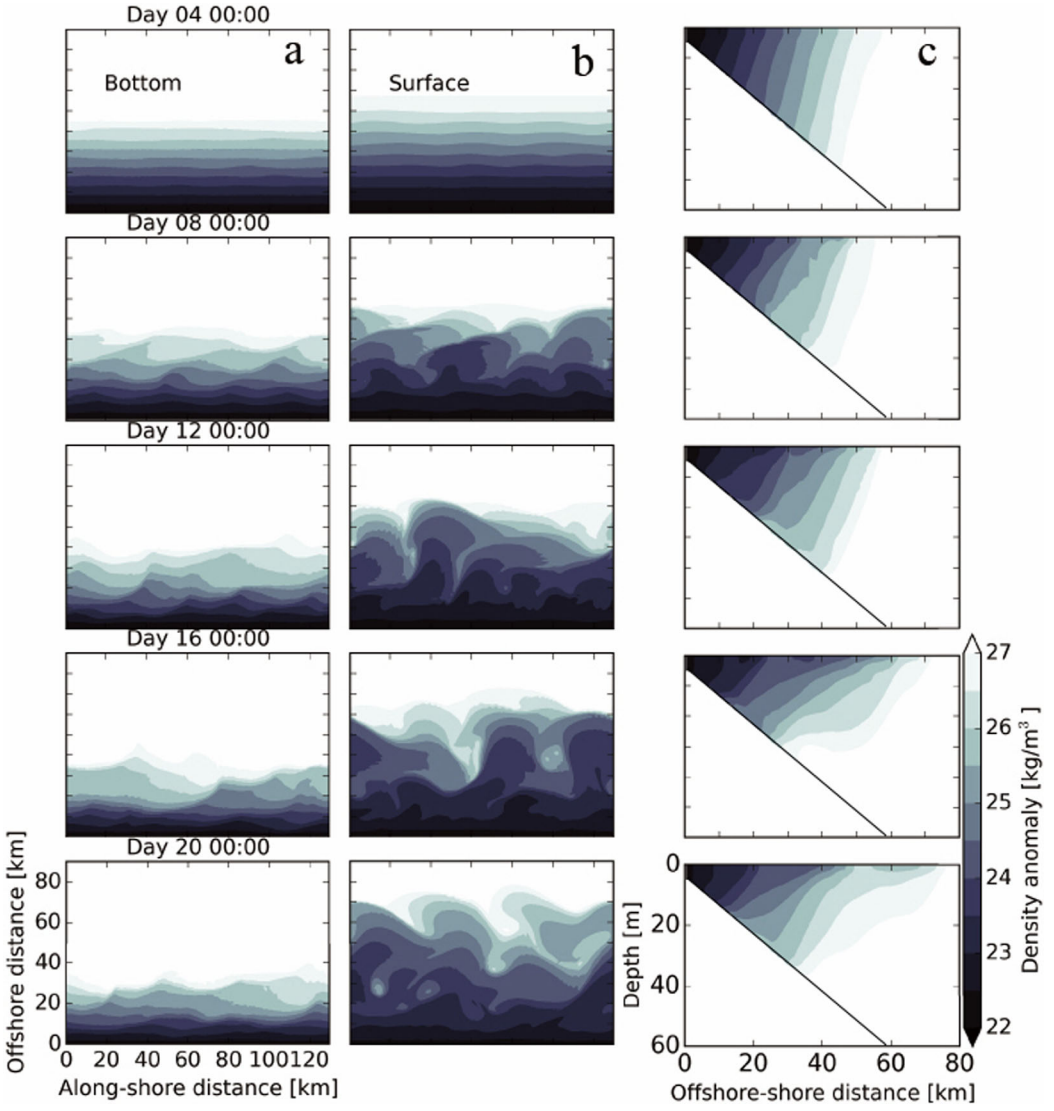

Figure 3. (a) Bottom density distribution, (b) surface density distribution during the evolution of baroclinic eddies for run 2, and (c) the simultaneous cross-shore density structure for the same transect denoted by the red dashed line in Figure 2c. A density interval of 0.5 kg/m^3 is used for all the figures, also density ranges for all figures are identical.

implies a reduction in isopycnal slope, demonstrating the relaxation of the mean flow by the baroclinic eddies.

3.2. Near-Bottom Convergence and Water Age Analysis

Figure 4a shows a time series of flow convergence at the bottom along a cross-shore transect for run 6. Two migrating convergent zones are seen with a thin divergent zone in between. The first convergence starts to form and strengthens on day 2; the bottom boundary layer thickens simultaneously as convergence develops. Low-age water is pooled at the convergent zone with intense mixing, and in a couple of days, injected into the interior along the adjacent isopycnal. The convergent zone migrates to fresher isopycnals (shoreward in geographical sense). A second convergent zone generates around a couple of days later with similar characteristics of bottom boundary layer behaviors, and intrusion of low-age water also forms with a lag of around a couple of days. These low-age tongues migrate inshore and last for around 10 days till day 16, that is, when the convergent flows become too weak and intrusions are halted.

Transects of simulated water age, tracer concentration, and simultaneous vertical stratification at certain evolution stage of the flow are shown in Figures 4b–4d for the same run. Water age at the bottom is zero

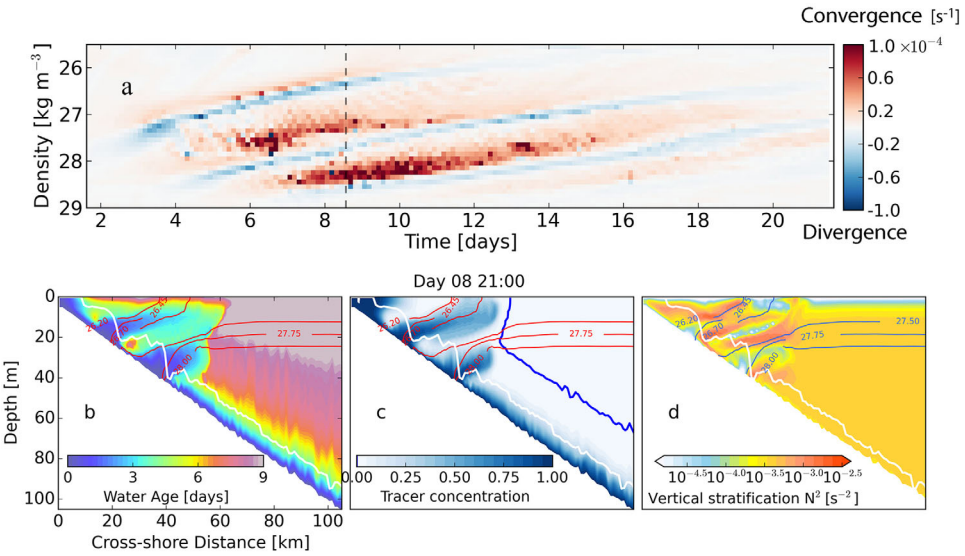

Figure 4. (a) Time series of convergent flow in density coordinates from run 6. Red represents convergence that associated with a net gain of water; blue represents divergence that associated with a net loss of water. Cross-shore section of (b) simulated water age, (c) simulated tracer concentration, and (d) vertical stratification on day 8; the transect is denoted by the red dashed line as shown in Figure 2c. The white lines represent the top of the bottom boundary layer; the blue line in Figure 4c denotes tracer concentration $C = 0.0001$; and the identical isolines in Figures 4b–4d are density levels.

because the tracer source is released at the bottom. The blue line in Figure 4c denotes tracer concentration $C = 0.0001$. The region where water age is undefined is associated with tracer concentration, C, lower than 10^{-4}. Hereafter, region with undefined water age will be whitened. The bottom boundary layer, operationally defined as the layer in which the density change is less than 0.5 kg m^{-3} from the bottom, is a near-bottom, thin and well-mixed layer known to exchange water with the interior water column in places where concentrated isopycnal intersects the seafloor (e.g., Houghton & Visbeck, 1998; Pickart, 2000; Pinkel, 1997; Zhang et al., 2015).

Water age in the water column quantifies the connection between water at the bottom and that in the upper layers, and multiple low-age intrusions, in response to the convergent flow, spread into the interior. Low water age indicates intense exchange or transport from the bottom to a location. Two resulting low-age intrusions, lower than 3 days, spread along layers that are characterized by low vertical stratification, shoaling toward the surface. A thickening in the bottom boundary layer is seen at the foot of each intrusion. This is similar to the "bottom boundary layer detachment" described by Pickart (2000). Two concentrated isopycnal zones form, which are the immediate offshore edges of the two intrusions. The bottom boundary layer thins beyond these immediate offshore edges, indicating the attenuation of mixing at the locations. These characteristics of bottom properties in the middle water column are similar to what previous studies detected (Barth et al., 1998; Houghton & Visbeck, 1998; Pickart, 2000; Zhang et al., 2015).

3.3. Vertical Flux Due to Bottom Convergence

To quantitatively investigate the strength of intrusions, tracer fluxes through a reference plane above the bottom are calculated following equation (16). Figures 4b and 4d indicate that low-age water spreads into the interior following a layer that is characterized by degraded vertical stratification, otherwise is confined underneath the bottom boundary layer within an average of 5 m above the bottom. Therefore, it is reasonable to assume that bottom tracer extended into the interior is predominantly controlled by the dynamics of the intrusions.

Figure 5a shows a transect of the simulated density field superimposed with the current filed, cross-shore versus vertical velocity. The current field suggests that water converges at the location where the bottom boundary layer thins, which is most likely the offshore edge of the convergent zone. The convergence-influenced regions emerge as of characterized by prominent vertical velocity, which reduces quantitatively

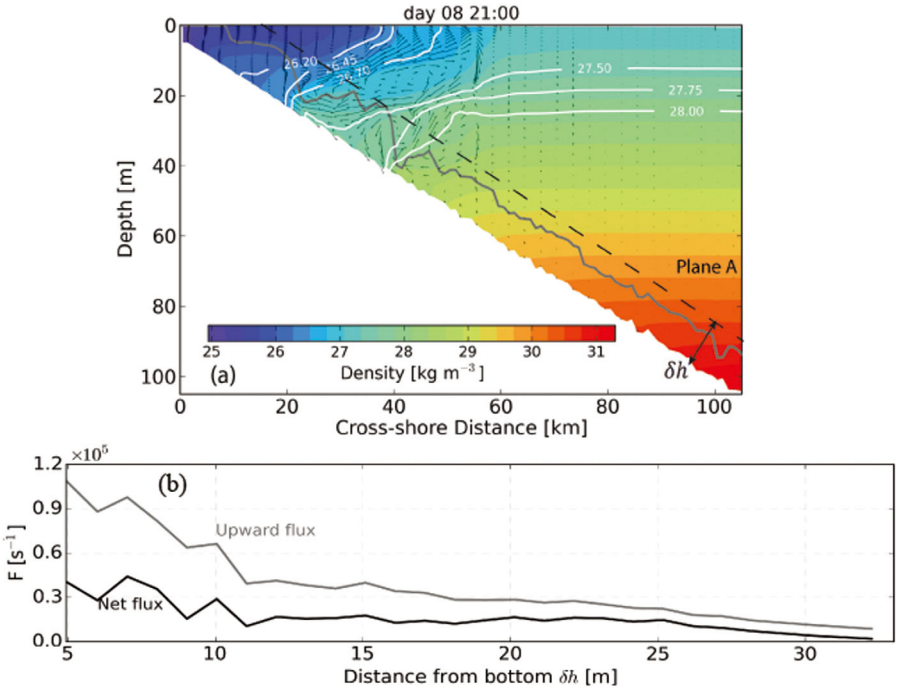

Figure 5. (a). Cross-shore section of simulated density superimposed with velocity field, cross-shore versus vertical velocity, for the same transect and the same time as shown in Figure 4. The gray line denotes the top of the bottom boundary layer, and the white isolines are the identical density levels as shown in Figure 4. The black dashed line is a reference plane, and δh is the distance between the bottom and this plane. (b) Upward flux (gray line) and net flux (black line) through plane A on the basis of δh.

as shoaling since mixing effect degrades in the pathway (Figure 4d). Figure 5b shows the upward tracer flux and net vertical flux on the basis of a variety of δh, both gradually decrease shoaling.

3.4. Impact of the Horizontal Slope Burger Number

In consideration of the analysis of model results, convergence consequently generates in response to baroclinic eddy triggered lateral buoyancy transport (Figure 4a). The evolution of the density field reveals that under a small initial horizontal slope Burger number, baroclinic eddies develop fast and are accompanied by severe on- and offshore isopycnal motions. The intensity of these features degrades with enhanced horizontal slope Burger number (S_H) until eddy structure disappears, and cross-shore isopycnal motions become rather trivial; this is when S_H exceeds a threshold (i.e., $\gtrsim$0.2 with a few exceptions in association with $Ri = 1$, based on Hetland (2016)). Figure 6 shows extent of distortion of isopycnals near the bottom layer, providing a visible assessment for the development of baroclinic instabilities in the light of S_H impacts. The time at which each case is shown is corresponding to the normalized time $t' = 50$. Significant distortions imply intense baroclinic eddies, which triggers lateral buoyancy transport. In contrast, suppressed distortion indicates inhibited buoyancy transport. Figure 6 indicates that small S_H gives rise to intense buoyancy transport near the bottom, suggesting the occurrence of convergent flows.

Following the above, comparisons of convergent flows between different runs are shown in Figure 7 (in dimensional time). The convergent flow, ξ, scales substantially as $\frac{U}{L}$, where U is the horizontal velocity scale and L is the horizontal length scale; $U \sim \frac{M^2 H}{f}$ in accordance to thermal wind relation, where H is the vertical length scale. Thus $\xi \sim \frac{M^2 H}{fL} = A\frac{M^2}{f}$ with a constant $A = \frac{H}{L}$, indicating the strength of convergent flow is proportional to the ratio of initial horizontal stratification to Coriolis parameter. To compare different runs, the convergent flows are normalized by initial $\frac{M^2}{f}$. Figure 7 shows time series of normalized convergent flow (ξ^*) in density coordinates for different runs, which illustrates behavioral differences in response to S_H values. Random localized convergent zones form, nevertheless, convergence becomes extremely weak with increased S_H.

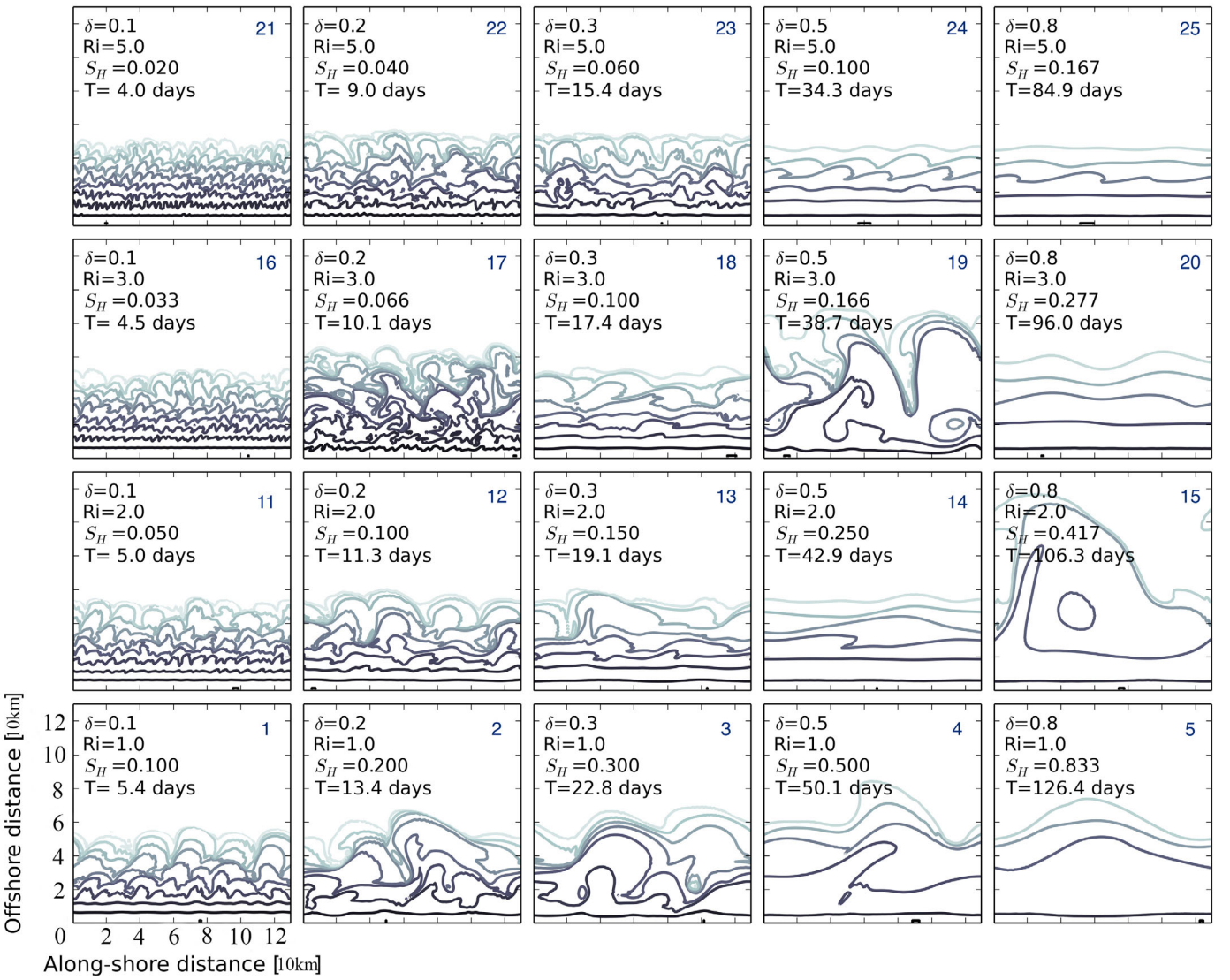

Figure 6. Simulated bottom density distribution at $t'=50$ for different cases, and the run number is labeled for each figure. A constant density interval, 0.5 kg/m^3, is used. Since the density range varies between different runs, indications of the value of the isopycnals are not shown in this figure. Nevertheless, the shadings of the isoline are consistent such that dark colors represent fresh waters and light colors represent dense waters.

The time scale for intrusion generation differs between runs, Figure 8 shows the time when the intrusions are most severe for runs in association with $Ri = 1$, and Figure 9 shows water age at $t'=50$ for runs in association with a variety of Richardson number values. Multiple intrusions can form under small horizontal slope Burger number, while intrusion barely forms under large horizontal slope Burger number. The evolution of water age is consistent with convergent flows; the characteristics of the occurrence of bottom water intrusions vary substantially between runs (Figures 7–9). It takes longer for runs associated with large horizontal slope Burger number to generate an intrusion and reach its maximum transport, and an intrusion barely generates when the convergence is weak.

Horizontal stratification vanishes offshore of 50 km, the water column is relatively stable, and near-bottom motions are inhibited, such that the bottom boundary layer is generally thick and absent of lateral variability. On the other hand, inshore of around 10 km, water is extremely well mixed and properties are homogenous, hence the top of the bottom boundary layer often emerges at the surface. Both of those are not the regions of interest during comparisons, by contrast, the region in between is the domain we focus on for comparisons. Intense mixing can erode the upper reach of the bottom boundary layer upward and thicken

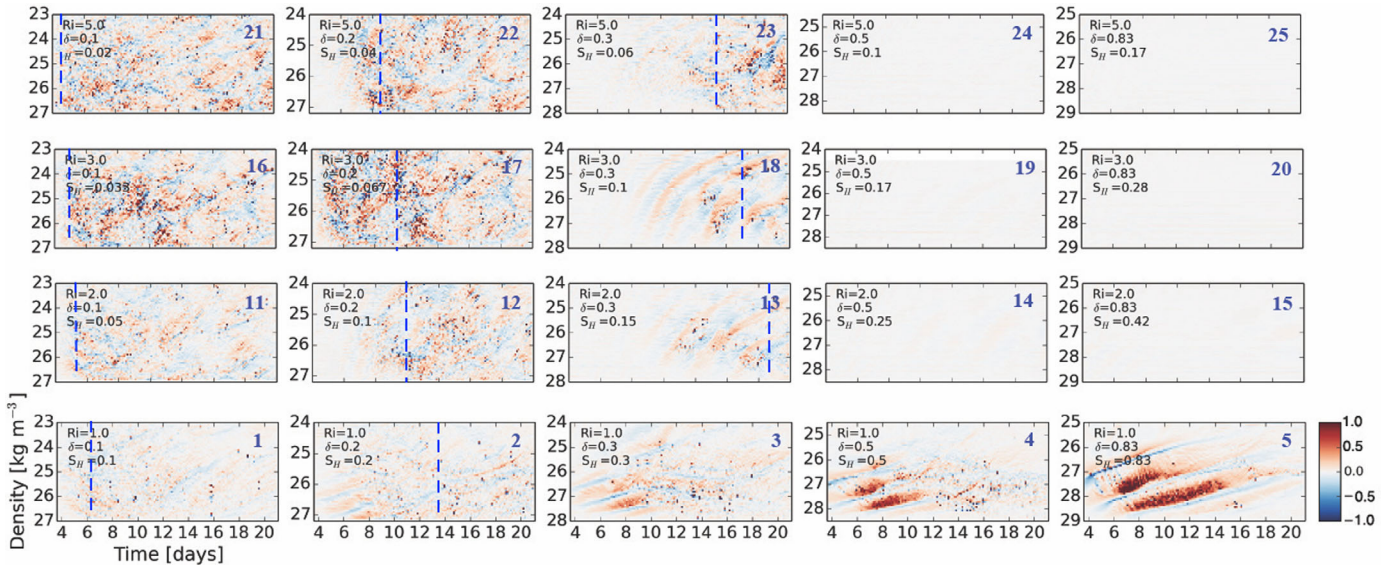

Figure 7. The same information as shown in Figure 4a, associated with different values of horizontal slope Burger number. To compare different cases, the convergent flows ($\times 10^4 s^{-2}$) are normalized by initial $\frac{M^2}{f}$. The run numbers are labeled accordingly based on Table 1. The dashed blue lines denote the dimensional time corresponding to $t'=50$. The dashed blue lines are absent in a subset of the cases because the dimensional time corresponding to $t'=50$ exceeds the given time series range.

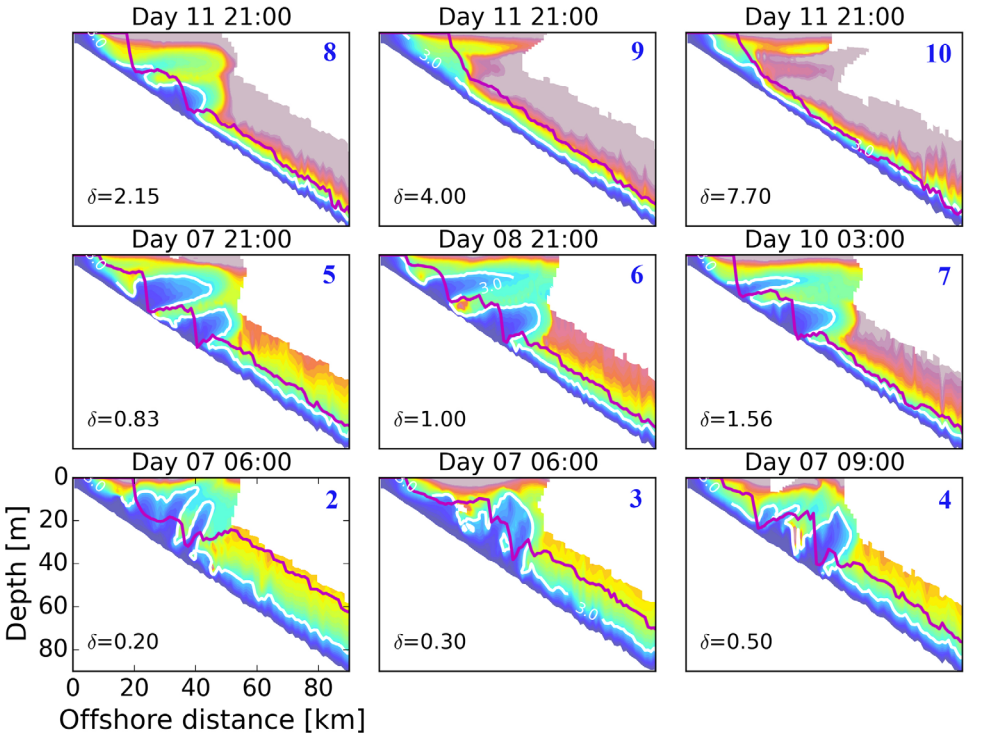

Figure 8. Cross-shore sections of simulated water age at the maximum intrusion time for a subset of the runs. Note that the same time as run 8 is used for runs 9 and 10. Since the dimensional time that each run performed is different (see Table 1), the scales of the shading of the runs take a variety of ranges. Instead of adding a colorbar for each run, a white line that denotes the water age of 3 days is superimposed in each figure. The magenta lines denote the top of bottom boundary layer.

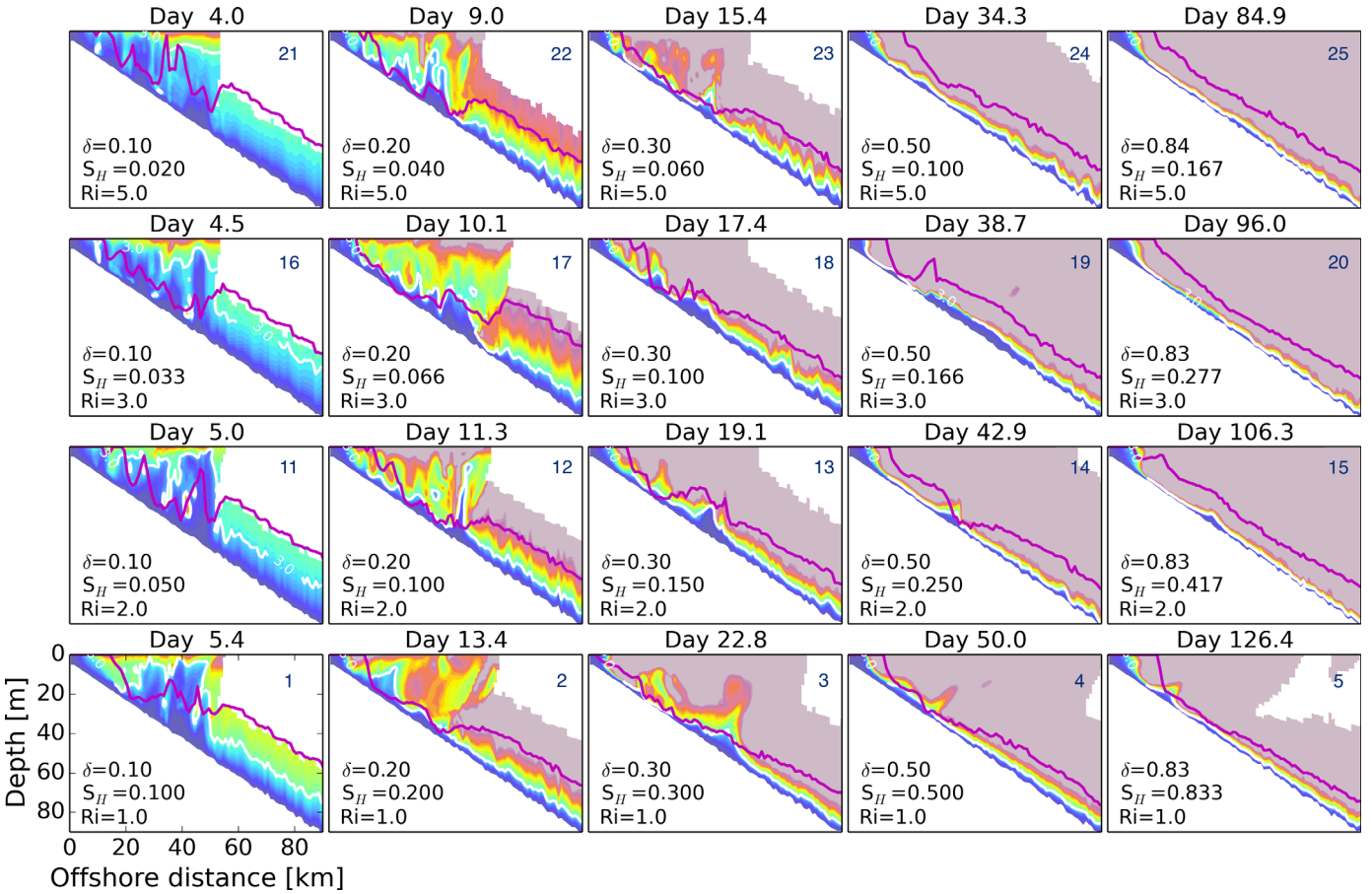

Figure 9. The same information as shown in Figure 8, at $t' = 50$, in association with different Richardson number values.

the bottom boundary layer. Previous studies relate mixing to buoyancy and momentum transport across-isopycnal surfaces in estuarine and coastal regions (Horner-Devine et al., 2015; Ivey et al., 2008; Sherman et al., 1978; Stacey et al., 2011). Such that intense mixing, thus lateral buoyancy transport, occurs at the locations where thickening in bottom boundary layer emerges. The characteristics of the bottom boundary layer behavior disappear in a subset of the runs, indicating the inhibited mixing at the bottom and the vanish of intrusions (Figures 8 and 9).

Normalized bottom material fluxes are compared quantitatively, and results demonstrate that intense convergent flow leads to severe bottom water intrusions and vice versa (Figures 7–9). Here we assume that the maximum flux operationally represents the typical intensity of flux associated with each run. Scale analysis suggests the upward and net fluxes are also proportional to the ratio of initial horizontal stratification to Coriolis parameter, to be consistent, the fluxes are normalized before comparisons between different runs. Figure 10a shows S_H versus the normalized maximum upward flux on logarithmic scales, and Figure 10b shows S_H versus the normalized maximum net flux on logarithmic scales; the red dashed lines in both figures denote the criterion of S_H (0.2, based on Hetland (2016)). Fluxes decrease linearly with increased horizontal slope Burger number except for a subset of the simulations in association with large Richardson number, which fall off the linear trend.

4. Discussions

Water age simulations indicate that lateral buoyancy transport in response to baroclinic eddies can induce convergence at the bottom, which consequently causes upward extension of bottom material (Figures 4 and 8). In agreement with previous studies (Barth et al., 1998; Houghton & Visbeck, 1998; Pickart, 2000;

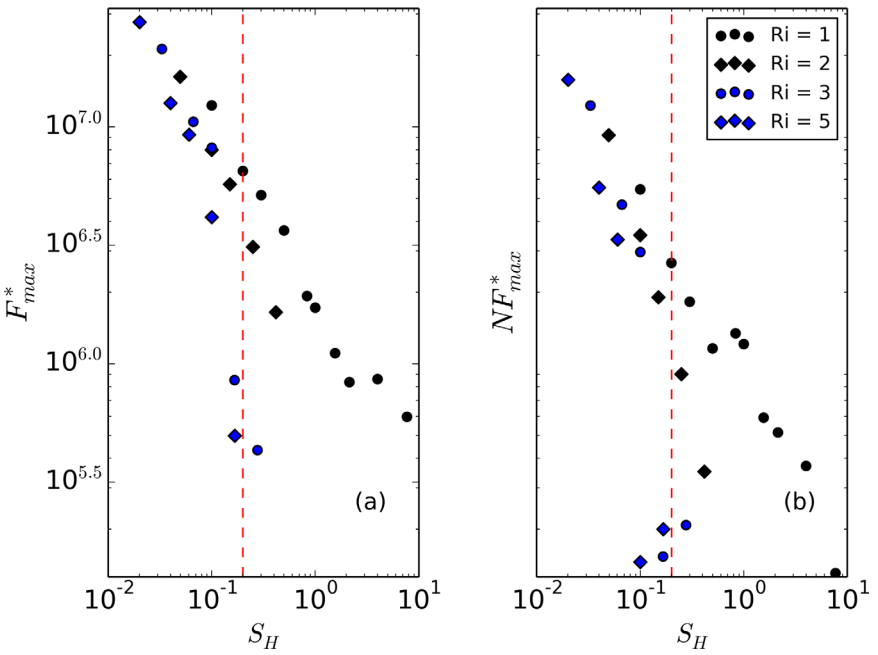

Figure 10. (a) Horizontal slope Burger number versus the normalized maximum upward tracer flux (s^{-2}). (b) Horizontal slope Burger number versus the normalized maximum net tracer flux (s^{-2}). These both are on logarithmic scales, and the dashed lines denote a criterion of 0.2 for horizontal slope Burger number.

Zhang et al., 2015), this study demonstrates that an upward bottom material flux often accompanies the buoyancy transport induced convergent flow near the bottom. However, mechanisms that trigger the buoyancy transport differ. The resulting buoyancy arrest in previous studies is prominently Ekman transport induced (e.g., Chapman & Lentz, 1994; Houghton & Visbeck, 1998), and lateral buoyancy transport in this study is a consequential effect of baroclinic eddies.

Three week time series of the normalized convergent flows associated with a variety of Richardson number are illustrated in dimensional time, superimposed with the dashed blue lines denoting the time corresponding to $t'=50$ (Figure 7). Convergent flow induced bottom intrusions can have important implications for local biogeochemistry. Re-suspension of bottom materials associated with the intrusions fertilizes the surface and can drive new primary production. Hypoxia is an ecological phenomenon that often occurs seasonally at coastal regions like Texas-Louisiana shelf and causes undesired consequences (Rabalais et al., 2002). Respiration and organic matter decay consume oxygen, which may cause hypoxia formation under certain condition like inhibited ventilation. Existing hypoxic water at the bottom can spread into the interior following the intrusions. Both the new primary production and hypoxic water can form episodic patchinesses in response to the nature of eddies (e.g., Capet et al., 2008a, 2008b).

Convergence migrates to fresher isopycnal (inshore in a geographical sense) over time persistently in all runs (Figure 7). Buoyancy transport in response to baroclinic eddies causes reduction in isopycnal slope, and will be shut down once the relaxation of isopycnal completes. The resulting convergence also vanishes once buoyancy transport ceases. The relaxation of sloped isopycnal would complete from the deep upward, which indicates that the vanishing in lateral buoyancy transport at depth would occur prior. This can explain the inshore migration of convergence. On the other hand, convergence induced by relatively stable Ekman transport is expected to migrate to denser isopycnal before buoyancy arrest can occur.

In contrast to the single stationary intrusion described by previous studies (e.g., Chapman & Lentz, 1994; Houghton & Visbeck, 1998), multiple localized convergent zones can form, and the consequent intrusions are generally transient in this study. Numerical studies of downslope Ekman transport and buoyancy arrest theory above stratified fluid and slopping bottom have been widely extended (e.g., Brink & Lentz, 2010b; Chapman & Lentz, 1994; Lentz & Trowbridge, 1991; Yankovsky & Chapman, 1997). A front system similar to the shelf-break front in the Middle Atlantic Bight is stationary and convergence of buoyancy transport occurs at the shoreward side of the foot of the front. One stationary intrusion abutting the frontal isopycnal

generates (Barth et al., 1998; Chapman & Lentz, 1994; Houghton & Visbeck, 1998). Frontogenesis also occurs over the Texas-Louisiana shelf; however, buoyancy transport over the shelf varies due to the redistribution of freshwater introduced from the Mississippi River system (Cho et al., 1998; Cochrane & Kelly, 1986; DiMarco et al., 2010). Instead of a stationary system (buoyancy arrest), buoyancy front in this region is more variable, and the consequent intrusions are relatively transient. The eddy structures in the vicinity of river plume front regions over the Texas-Louisiana shelf suggest the development of instability (Zhang et al., 2015, Figure 1). In this study, isopycnals slightly concentrate at the location where bottom boundary layer thins to form a transient front. Figures 4, 8, and 9 show that multiple low-age intrusions can form simultaneously, which is due to the nature of baroclinic eddies.

The intensity of bottom convergence and tracer fluxes is determined by horizontal slope Burger number (S_H). Small S_H corresponds to large isopycnal slope, which is proportional to available potential energy that feeds the growth of baroclinic eddies. The intense convergent flow associated with runs like 1 and 2 is usually chaotic due to the high variability (Figure 7). The associated low-age intrusions generate and emerge at the surface frequently. Increased S_H mitigates the intensity of convergent flow and bottom intrusion, because for runs with large S_H, eddies that can generate convergence are weaker, and the consequent buoyancy transport is inhibited, therefore diapycnal motion near the bottom is about to be restricted. Thus convergence at the bottom tends to vanish once S_H is beyond 0.2. This study suggests the bottom material flux (ultimately manipulated by baroclinic instability induced eddy transfer) varies in response to local horizontal slope Burger number. The subset that falls off the linear trend in Figure 10 suggests suppression of baroclinic instability. In contrast to a threshold of $S_H \gtrsim 0.2$ as given in Hetland (2016), tracer fluxes indicate that the threshold for suppression of baroclinic instability varies slightly with Richardson number, decreasing with increased Richardson number and vice versa.

The fundamental similarity between runs is that bottom water spreads into the interior to form an intrusion along a layer that is characterized by degraded vertical stratification (Figure 4d). Intense mixing is underway at the convergent zone and results in a thickening in the bottom boundary layer, which is expressed as "bottom boundary layer detachment" by Pickart (2000). The concentrated isopycnals act as a density barrier and thin the bottom boundary layer at the edge of the intrusion, where a reversal in bottom alongshore velocity occurs (Figure 11). The bottom boundary layer in association with small S_H does show slight

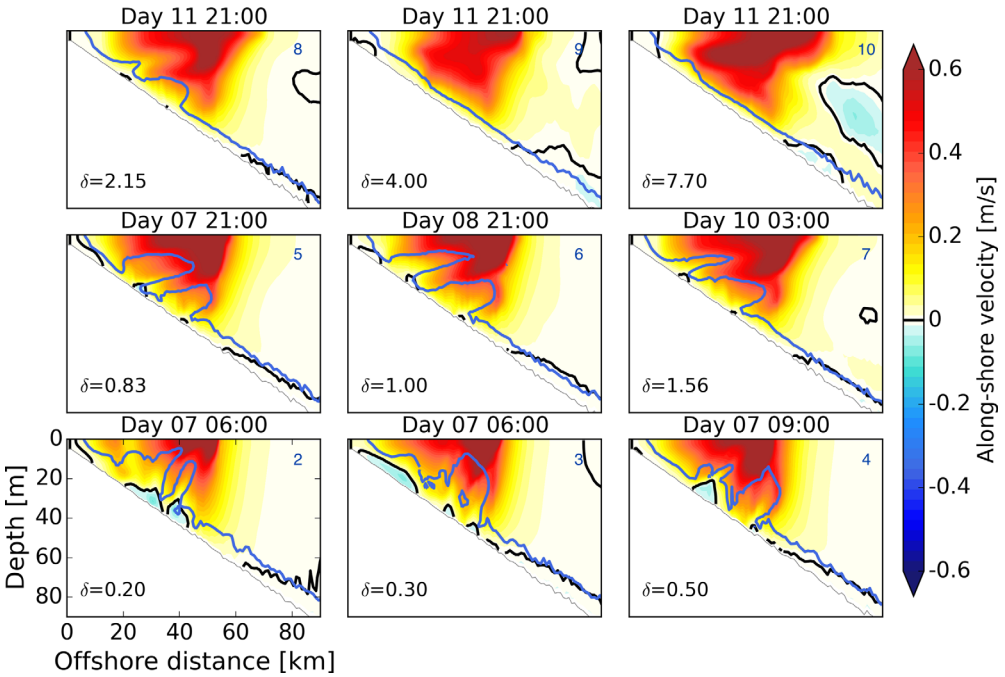

Figure 11. Alongshore velocity for a cross section of runs in association with $Ri = 1$. The black line represents zero alongshore velocity, and the blue line represents water age of 3 days. Note that the same cross section and same time as shown in Figure 8 are used.

behavioral differences due to the vigorous baroclinic eddies and chaotic convergence. Figures 8 and 11 suggest that in response to large S_H, the characteristics of bottom boundary layer behavior and the reversal in bottom alongshore velocity vanish (inshore of 50 km).

5. Summary

This study demonstrates that baroclinic instability is of importance in lateral buoyancy transport, this is in agreement with previous studies (e.g., Haine & Marshall, 1998). Different from Houghton and Visbeck (1998), Barth et al. (1998), and Zhang et al. (2015), intrusions reproduced in this simple three-dimensional model are induced by convergence of buoyancy transport in response to baroclinic eddies. Water age is introduced to provide a visible assessment for the location of convergent zone and the associated upward extension of bottom water. Multiple localized convergent zones can form, and intrusions are extremely transient due to the highly variable convergence. Generally, the low-age water spreads upward abutting a layer that is characterized by degraded vertical stratification. The bottom boundary layer thickens under intense mixing at the convergent zone, and thins beyond the offshore edge of the intrusion, where isopycnal slightly concentrates and acts as a barrier.

The intensity of bottom convergence and tracer fluxes is determined by horizontal slope Burger number (S_H). The adequate available potential energy associated with small S_H results in vigorous baroclinic eddies and chaotic convergent flow, such that low-age intrusions are extremely transient. Those intrusions shoal in the interior and frequently emerge at the surface. The chaotic convergent flow due to energetic system and the extremely transient intrusions mitigate when S_H increases. Baroclinic instability is suppressed when S_H is beyond a threshold, convergence becomes trivial and intrusions barely form. Fluxes of bottom material decrease linearly with S_H on logarithmic scales (Figure 10), nevertheless, fluxes in association with a subset of the simulations fall off the linear trend since baroclinic instability is suppressed under the given values for S_H (runs 19, 20, 24, and 25).

This study suggests that shelf features determine the characteristics of lateral buoyancy transport in response to barcolinic eddies. The setup of this three-dimensional model has the potential portability to evaluate flux intensity due to baroclinic instability with parameters specifically adapted for a shelf. The eddy induced convergent flow has important implications on the concentration of material in the upper layer and the biogeochemistry of the shelf. These processes can be relevant qualities and are essential to the shelf biogeophysical dynamics.

Acknowledgments
Thanks go to the two anonymous reviewers for their insightful suggestions on improving the manuscript. This is a pure numerical study, and no original data were used. This work was funded by NOAA-CSCOR NGOMEX NA09N0S4780208.

References

Barth, J. A., Bogucki, D., Pierce, S. D., & Kosro, P. M. (1998). Secondary circulation associated with a shelfbreak front. *Geophysical Research Letters*, *25*(15), 2761–2764.

Brink, K. H., & Lentz, S. J. (2010a). Buoyancy arrest and bottom Ekman transport: Part II, Oscillating flow. *Journal of Physical Oceanography*, *40*, 636–655.

Brink, K. H., & Lentz, S. J. (2010b). Buoyancy arrest and bottom Ekman transport, Part I, Steady flow. *Journal of Physical Oceanography*, *40*, 621–635.

Capet, X., McWilliams, J. C., Molemaker, M. J., & Shchepetkin, A. F. (2008a). Mesoscale to submesoscale transition in the California Current System. Part I: Flow structure, eddy flux, and observational tests. *Journal of Physical Oceanography*, *38*, 29–43.

Capet, X., McWilliams, J. C., Molemaker, M. J., & Shchepetkin, A. F. (2008b). Mesoscale to submesoscale transition in the California Current System. Part II: Frontal processes. *Journal of Physical Oceanography*, *38*, 44–64.

Capet, X., McWilliams, J. C., Molemaker, M. J., & Shchepetkin, A. F. (2008c). Mesoscale to submesoscale transition in the California Current System. Part III: Energy balance and flux. *Journal of Physical Oceanography*, *38*, 2256–2269.

Chapman, D. C. (1985). Numerical treatment of cross-shelf open boundaries in a barotropic coastal ocean model. *Journal of Physical Oceanography*, *15*(8), 1060–1075.

Chapman, D. C., & Lentz, S. J. (1994). Trapping of a coastal density front by the bottom boundary layer. *Journal of Physical Oceanography*, *24*, 1464–1479.

Cho, K., Reid, R. O., & Nowlin, W. D. (1998). Objectively mapped stream function fields on the Texas-Louisiana shelf based on 32 months of moored current meter data. *Journal of Geophysical Research*, *103*(C5), 10377–10390.

Cochrane, J. D., & Kelly, F. J. (1986). Low-frequency circulation on the Texas-Louisiana continental shelf. *Journal of Geophysical Research*, *91*(C9), 10645–10659.

Cushman-Roisin, B., & Beckers, J. (2011). *Introduction to geophysical fluid dynamics: Physical and numerical aspects*. Cambridge, MA: Academic Press.

Deleersnijder, E., Campin, J. M., & Delhez, E. J. M. (2001). The concept of age in marine modelling: I. Theory and preliminary model results. *Journal of Marine Systems*, *28*, 229–267.

Delhez, E. J. M., Campin, J. M., & Deleersnijder, E. (1999). Toward a general theory of the age in ocean modelling. *Ocean Modelling*, *1*, 17–27.

Delhez, E. J. M., & Deleersnijder, E. (2006). The boundary layer of the residence time field. *Ocean Dynamics*, *56*, 139–150.

DiMarco, S. F., Chapman, P., Walker, N., & Hetland, R. D. (2010). Does local topography control hypoxia on the eastern Texas–Louisiana shelf? *Journal of Marine Systems*, *80*, 25–35.
Flather, R. A. (1976). A tidal model of the northwest Euopean continental shelf. *Memoires de la Societe Royale des Sciences de Liege*, *10*(6), 141–164.
Haine, T. W., & Marshall, J. (1998). Gravitational, symmetric, and baroclinic instability of the ocean mixed layer. *Journal of Physical Oceanography*, *28*, 634–658.
Hetland, R. D. (2016). Suppression of baroclinic instabilities in buoyancy-driven flow over sloping bathymetry. *Journal of Physical Oceanography*, *47*, 49–68.
Horner-Devine, A. R., Hetland, R. D., & MacDonald, D. G. (2015). Mixing and transport in coastal river plumes. *Annual Review of Fluid Mechanics*, *47*, 569–594.
Houghton, R. W., & Visbeck, M. (1998). Upwelling and convergence in the Middle Atlantic Bight shelfbreak front. *Geophysical Research Letters*, *25*(15), 2765–2768.
Ivey, G. N., Winters, K. B., & Koseff, J. R. (2008). Density stratification, turbulence, but how much mixing? *Annual Review of Fluid Mechanics*, *40*, 169–184.
Lentz, S. J., & Trowbridge, J. H. (1991). The bottom boundary layer over the Northern California shelf. *Journal of Physical Oceanography*, *21*, 1186–1201.
Mahadevan, A. (2014). Ocean science: Eddy effects on biogeochemistry. *Nature*, *506*, 168–169.
Mahadevan, A. (2016). The impact of submesoscale physics on primary productivity of plankton. *Annual Review of Marine Science*, *8*, 161–184. https://doi.org/10.1146/annurev-marine-010814-015912
Mahadevan, A., & Archer, D. (2000). Modeling the impact of fronts and mesoscale circulation on the nutrient supply and biogeochemistry of the upper ocean. *Journal of Geophysical Research*, *105*(C1), 1209–1225.
Mahadevan, A., D'Asaro, E., Lee, C., & Perry, M. J. (2012). Eddy-driven stratification initiates north Atlantic spring phytoplankton blooms. *Science*, *337*, 54–58.
McWilliams, J. C., Colas, F., & Molemaker, M. J. (2009). Cold filamentary intensification and oceanic surface convergence lines. *Geophysical Research Letters*, *36*, L18602. https://doi.org/10.1029/2009GL039402
Pickart, R. S. (2000). Bottom boundary layer structure and detachment in the shelfbreak jet of the Middle Atlantic Bight. *Journal of Physical Oceanography*, *30*, 2668–2686.
Pinkel, R. (1997). *Observations of coherent structures in the oceanic boundary layer* (AD-a333 292). Scripps Institution of Oceanography La Jolla CA Marine Physical Lab.
Rabalais, N. N., Turner, R. E., & Wiseman, W. J., Jr. (2002). Gulf of Mexico hypoxia, A.K.A. "The Dead Zone. *Annual Review of Ecology and Systematics*, *33*, 235–263.
Sherman, F., Imberger, J., & Corcos, G. (1978). Turbulence and mixing in stably stratified waters. *Annual Review of Fluid Mechanics*, *10*, 267–288.
Siegel, D., McGillicuddy, D. J., & Fields, E. A. (1999). Mesoscale eddies, satellite altimetry, and new production in the Sargasso Sea. *Journal of Geophysical Research*, *104*(C6), 13359–13379.
Smith, K. M., Hamlington, P. E., & Fox-Kemper, B. (2015). Effects of submesoscale turbulence on ocean tracers. *Journal of Geophysical Research*, *121*, 908–933. https://doi.org/10.1002/2015JC011089
Stacey, M. T., Rippeth, T., & Nash, J. D. (2011). Turbulence and stratification in estuaries and coastal seas. In E. Wolanski and D. McLusky (Eds.), *Treatise on estuarine and coastal science* (Vol. 2, pp. 9–36). Amsterdam, the Netherlands: Elsevier.
Yankovsky, A. E., & Chapman, D. C. (1997). A simple theory for the fate of buoyant coastal discharges. *Journal of Physical Oceanography*, *27*, 1386–1401.
Zhang, W., Hetland, R. D., DiMarco, S. F., & Fennel, K. (2015). Processes controlling mid-water column oxygen minima over the Texas-Louisiana shelf. *Journal of Geophysical Research*, *120*, 2800–2812. https://doi.org/10.1002/2014JC010568
Zhang, W. G., Wilkin, J. L., & Schofield, O. M. E. (2010). Simulation of water age and residence time in New York Bight. *Journal of Physical Oceanography*, *40*(5), 965–982.